Contrib. Astron. Obs. Skalnaté Pleso **56/2**, 36 – 54, (2026)
https://doi.org/10.31577/caosp.2026.56.2.36

Surface gravitational redshift of massive protoneutron stars: effects of σ^* and ϕ mesons

J.L. Huo[1], X.H. Wu[1], W.B. Ding[2] and X.F. Zhao[1]

[1] *School of Sciences, Southwest Petroleum University, Chengdu, 610500, China (E-mail: jlhuo2006@126.com)*

[2] *College of Physics and Electronic Information Engineering, Guangxi Minzu Normal University, Chongzuo, 532200, China*

Received: December 21, 2025; Accepted: February 16, 2026

Abstract. The effects of hyperon interactions (occurring through the coupling of hyperons to the σ^* and ϕ mesons) on the surface gravitational redshift z of proto-neutron stars (PNSs)—specifically PSR J0740+6620, PSR J0348+0432, PSR J1614-2230, and PSR J0737-3039A—are investigated using relativistic mean field theory. It is found that the increase in central pressure and central energy density due to hyperon interactions becomes more pronounced for higher-mass PNSs, while for lower-mass PNSs this effect is negligible. When hyperon interactions are included, the mass M, compactness M/R, and surface gravitational redshift z of a PNS all decrease at a given central energy density ε_c. For the higher-mass PNSs PSR J0740+6620 and PSR J0348+0432, the influence of hyperon interactions on compactness M/R and surface redshift z is significant. In contrast, for the lower-mass PNSs PSR J1614-2230 and PSR J0737-3039A, the effect on M/R and z is negligible.

Key words: stars: binaries – general: stars

1. Introduction

Neutron stars (NSs) possess extremely strong magnetic fields and rotate at very high speeds (Deng et al., 2021). Some of their intriguing properties may be explained by dark matter (Ding et al., 2022). NSs are very massive and have very small radii, resulting in extremely high densities, which significantly influence their properties (Mu et al., 2017; Li et al., 2021). Consequently, once the mass of a NS is determined, it is possible to infer certain characteristics of the star.

As early as 2004, the double NS system PSR J0737–3039 was discovered (Lyne et al., 2004). The NS PSR J0737–3039A has a typical NS mass, with reported values of $M = 1.337$ $M_\odot$ (Morrison et al., 2004) or $M = 1.3381 \pm 0.0007$ $M_\odot$ (Kramer et al., 2006).

NSs with exceptionally high masses have also been discovered in recent decades. The NS PSR J1614–2230, with a mass of $M = 1.97 \pm 0.04$ $M_\odot$, was identified in 2010 (Demorest et al., 2010). Its mass was later refined to $M =$

$1.93 \pm 0.07\ \mathrm{M}_\odot$ in 2016 (Fonseca et al., 2016). Subsequently, PSR J0348+0432, with a mass of $M = 2.01 \pm 0.04\,\mathrm{M}_\odot$, was found in 2013 (Antoniadis et al., 2013). An even more massive NS, PSR J0740+6620, with a mass of $M = 2.14^{+0.10}_{-0.09}\,\mathrm{M}_\odot$, was observed in 2020 (Cromartie et al., 2020). Its mass and radius were later precisely determined to be $M = 2.08^{+0.07}_{-0.07}\,\mathrm{M}_\odot$ by (Fonseca et al., 2021) and $R = 13.7^{+2.6}_{-1.5}$ km by (Miller et al., 2021) in 2021. Most recently, the NS PSR J0952–0607, with a record mass of $M = 2.35^{+0.17}_{-0.17}\,\mathrm{M}_\odot$, was discovered in 2022 (Romani et al., 2022).

These NSs are relatively massive, and their mass must constrain their properties. Therefore, measuring NS masses is crucial for determining their structure and internal properties. Although the massive NSs PSR J1614-2230, PSR J0348+0432, and PSR J0740+6620 are not the heaviest discovered to date, studying the influence of their precisely measured masses on their properties remains highly significant.

After a supernova, a NS is formed in the core. Prior to that, a proto-neutron star (PNS) emerges, which can reach temperatures as high as 30 MeV. Subsequently, the PNS cools via neutrino emission and evolves into a NS (Burrows & Lattimer, 1986). Thus, the study of PNSs is important for understanding the formation and evolution of NSs.

In theoretical research, we can compare PNS evolutionary models with observational data of cold NSs. The purpose of this comparison is not to directly equate the transient and steady states, but rather to leverage the continuous physical link—from the hot PNS to the cold NS—established by theoretical models. By contrasting the initial/early stages of the evolutionary trajectory with the final/observed state, we aim to jointly constrain the microphysics of dense matter.

The description of NS matter can incorporate σ, ω, and ρ mesons to represent the interaction between nucleons (Glendenning, 1997), while interactions between hyperons can be described by the mesons $f_0(1020)$ (denoted as σ^*) and $\phi(975)$ (denoted as ϕ) (Schaffner et al., 1994).

Closely related to the mass and radius of a NS is the surface gravitational redshift, which depends directly on the compactness M/R (Glendenning, 1997). Therefore, studying the surface gravitational redshift of NSs is as important as investigating their compactness.

In this work, we employ relativistic mean field (RMF) theory (Zhou, 2016) with the baryon octet to examine the influence of the σ^* and ϕ mesons on the surface gravitational redshift of massive PNSs PSR J0740+6620, PSR J0348+0432, and PSR J1614-2230. For comparison, we also calculate the surface gravitational redshift of the typical-mass PNS PSR J0737-3039A.

2. RMF theory at finite temperature: the infinite system

The Lagrangian density of infinite nuclear matter is as follows (Glendenning, 1997)

$$\begin{aligned}\mathcal{L} = & \sum_B \overline{\Psi}_B(i\gamma_\mu\partial^\mu - m_B + g_{\sigma B}\sigma + g_{\sigma^* B}\sigma^* \\ & -g_{\omega B}\gamma^0\omega - g_{\phi B}\gamma^0\phi - g_{\rho B}\gamma^0\tau_3\rho)\Psi_B \\ & -\frac{1}{2}m_\sigma^2\sigma^2 - \frac{1}{3}g_2\sigma^3 - \frac{1}{4}g_3\sigma^4 \\ & +\frac{1}{2}m_\omega^2\omega^2 + \frac{1}{2}m_\rho^2\rho^2 - \frac{1}{2}m_{\sigma^*}^2\sigma^{*2} + \frac{1}{2}m_\phi^2\phi^2 \\ & + \sum_{\lambda=e,\mu} \overline{\Psi}_\lambda \left(i\gamma_\mu\partial^\mu - m_\lambda\right)\Psi_\lambda. \end{aligned} \tag{1}$$

Given neutrino binding, the baryonic partition function of infinite nuclear matter at finite temperature is

$$\begin{aligned} lnZ_B = & \frac{V}{T}\langle\mathcal{L}\rangle + \sum_B \frac{2J_B+1}{2\pi^2} \\ & \int_0^\infty k^2 dk \left\{ ln\left[1 + e^{-(\varepsilon_B(k)-\mu_B)/T}\right]\right\}. \end{aligned} \tag{2}$$

The total baryon number density (Glendenning, 1987a,b) is

$$\rho = \sum_B \frac{2J_B+1}{2\pi^2} b_B \int_0^\infty k^2 n_B(k) dk. \tag{3}$$

The energy density and the pressure of baryons and mesons respectively are

$$\begin{aligned} \varepsilon = & \frac{1}{2}m_\sigma^2\sigma^2 + \frac{1}{2}m_{\sigma^*}^2\sigma^{*2} + \frac{1}{3}g_2\sigma^3 + \frac{1}{4}g_3\sigma^4 \\ & +\frac{1}{2}m_\omega^2\omega_0^2 + \frac{1}{2}m_\phi^2\phi^2 + \frac{1}{2}m_\rho^2\rho_{03}^2 \\ & +\sum_B \frac{2J_B+1}{2\pi^2}\int_0^\infty \kappa^2 n_B(k)\mathrm{d}\kappa\sqrt{\kappa^2 + m_B^{*2}}, \end{aligned} \tag{4}$$

$$\begin{aligned} p = & -\frac{1}{2}m_\sigma^2\sigma^2 - \frac{1}{2}m_{\sigma^*}^2\sigma^{*2} - \frac{1}{3}g_2\sigma^3 - \frac{1}{4}g_3\sigma^4 \\ & +\frac{1}{2}m_\omega^2\omega_0^2 + \frac{1}{2}m_\phi^2\phi^2 + \frac{1}{2}m_\rho^2\rho_{03}^2 \\ & +\frac{1}{3}\sum_B \frac{2J_B+1}{2\pi^2}\int_0^\infty \frac{\kappa^4}{\sqrt{\kappa^2 + m_B^{*2}}} n_B(k) d\kappa. \end{aligned} \tag{5}$$

Here, $n_B(k)$ is the Fermi-Dirac distribution function of baryons

$$n_B(k) = \frac{1}{1 + exp\left[\left(\varepsilon_B(k) - \mu_B\right)/T\right]}. \tag{6}$$

If we don't take into account the interactions between leptons at finite temperatures, their partition function is

$$\begin{aligned} lnZ_L = & \frac{V}{T}\sum_i \frac{\mu_i^4}{24\pi^2}\left[1 + 2\left(\frac{\pi T}{\mu_i}\right)^2 + \frac{7}{15}\left(\frac{\pi T}{\mu_i}\right)^4\right] \\ & + V\sum_\lambda \frac{1}{\pi^2}\int_0^\infty k^2 dk\left\{ln\left[1 + e^{-(\varepsilon_\lambda(k) - \mu_\lambda)/T}\right]\right\}, \end{aligned} \tag{7}$$

the first line represents the contribution of massless neutrinos and the second line the contribution of electrons and μs.

The lepton number density is

$$\rho_l = \frac{1}{\pi^2}\int_0^\infty k^2 n_l(k) dk, \tag{8}$$

$$\rho_\nu = \frac{\pi^2 T^2 \mu_\nu + \mu_\nu^3}{6\pi^2}. \tag{9}$$

The energy density and the pressure of leptons are

$$\begin{aligned} \varepsilon &= \sum_l \frac{1}{\pi^2}\int_0^\infty \kappa^2 n_l(k) \mathrm{d}\kappa \sqrt{\kappa^2 + m_l^2} \\ &= \sum_\nu \left(\frac{7\pi^2 T^4}{120} + \frac{T^2\mu_\nu^2}{4} + \frac{\mu_\nu^4}{8\pi^2}\right), \end{aligned} \tag{10}$$

$$\begin{aligned} p &= \frac{1}{3}\sum_l \frac{1}{\pi^2}\int_0^\infty \frac{\kappa^4}{\sqrt{\kappa^2 + m_l^2}} n_l(k) d\kappa \\ &= \sum_\nu \frac{1}{360}\left(7\pi^2 T^4 + 30 T^2 \mu_\nu^2 + \frac{15\mu_\nu^4}{\pi^2}\right). \end{aligned} \tag{11}$$

The chemical potentials of baryons are

$$\mu_i = \mu_n - q_i\left(\mu_e - \mu_{\nu e}\right). \tag{12}$$

We can obtain the mass and the radius of a PNS through the Tolman-Oppenheimer-Volkoff (TOV) equation (Tolman, 1939; Oppenheimer & Volkoff, 1939)

$$\frac{\mathrm{d}p}{\mathrm{d}r} = -\frac{(p + \varepsilon)\left(m + 4\pi r^3 p\right)}{r\left(r - 2m\right)}, \tag{13}$$

$$m = 4\pi\int_0^r \varepsilon r^2 \mathrm{d}r, \tag{14}$$

$$M = m(R). \tag{15}$$

The TOV equations are only applicable to spherically symmetric, static (i.e., non-rotating and time-invariant) stellar objects. However, NSs are known to rotate very rapidly, and PNSs evolve rapidly over time. Neglecting rotation and temporal evolution will introduce certain errors. (1) The error from neglecting rotational effects depends mainly on the rotational speed. For slow rotation (period P$\geq$ 10 ms), the centrifugal force correction to the global structure (mass, radius) is approximately 1% to a few percent, and the TOV solution serves as a good approximation. For potentially extremely rapid rotation (P $\sim$ 1 ms), centrifugal support becomes significant and may lead to deviations exceeding 10% in mass and radius estimates, while also failing to describe stellar oblateness. This study aims to investigate the influence of the equation of state (EoS) within a static baseline; therefore, the spherical symmetry assumption is intentionally adopted to focus the problem. The spherical symmetry and static assumptions are limitations, and conclusions for rapidly rotating stars require further examination in axisymmetric models. (2) The error induced by neglecting temporal evolution. The TOV equations describe instantaneous hydrostatic equilibrium. During the middle and late stages of PNS evolution ($t > 1$ s), although temperature and composition change rapidly, the timescale for establishing hydrostatic equilibrium (milliseconds) is much shorter than the evolutionary timescale (10 seconds). The system can thus be considered to undergo a sequence of quasi-static equilibrium states. Therefore, our sequence of static solutions can be interpreted as potential 'snapshots' along the PNS cooling path. While this approach cannot self-consistently describe the evolutionary timescale, it clearly reveals the dependence of the structure on internal physical conditions. The dynamical phase of the very early stage (t $<$ 1 s) is beyond the applicable scope of this model. In summary, we adopt the simplified model in order to reveal the core physical mechanisms within a controlled framework and to provide a theoretical benchmark for more complex multidimensional time-dependent simulations.

The surface gravitational redshift of a PNS can be calculated by (Glendenning, 1997):

$$z = \frac{1}{\sqrt{1 - 2(M/R)}} - 1. \tag{16}$$

This formula is derived from the Schwarzschild metric, which holds valid above the surface of any star. Therefore, this formula is applicable to any relativistic star.

3. The parameters

We calculate the mass and radius of the PNSs using the following eight groups of nucleon coupling constants: DD-ME1 (Typel & Wolter, 1999), FSU2H (Tolos et al., 2017), FSU2R (Tolos et al., 2017), FSUGold (Todd-Rutel & Piekarewicz,

2005), GL85 (Glendenning, 1985), GL97 (Glendenning, 1997), GM1 (Glendenning & Moszkowski, 1991), and TW99 (Typel & Wolter, 1999).

The ratios of hyperon–hyperon coupling constants to nucleon–nucleon coupling constants can be defined as $x_{\sigma h} = \frac{g_{\sigma h}}{g_\sigma}$, $x_{\omega h} = \frac{g_{\omega h}}{g_\omega}$, $x_{\rho h} = \frac{g_{\rho h}}{g_\rho}$, where h denotes the hyperons Λ, Σ, and Ξ.

The coupling constant between ρ mesons and nucleons is derived from quark SU(6) symmetry (Schaffner & Mishustin, 1996; Schaffner-Bielich & Gal, 2000). The mass of a PNS increases with larger values of $x_{\sigma h}$ and $x_{\omega h}$ (Zhao, 2019). Consequently, to obtain the PNS mass, one must select sufficiently large values for these parameters. The theoretical baseline for the parameter $x_{\omega h}$ is approximately 0.667 (Glendenning, 1997). In phenomenological models, its typical variation range is about 0.5 to 1.0 (Weissenborn et al., 2012; Chatterjee & Vidana, 2016). To construct a viable model that includes hyperons while still yielding NSs with a mass of $\sim$2 $M_\odot$, it is necessary to adopt a larger value of $x_{\omega h}$ (i.e., a strong repulsive potential) to compensate for the softening of the EoS induced by the presence of hyperons. A value of $x_{\omega h} \sim 0.8$ is commonly required to satisfy this observational constraint (Weissenborn et al., 2012). Therefore, selecting 0.9 is reasonable and consistent with current observational limits. Within a more refined SU(3) flavor symmetry framework, the vector coupling constants for different hyperons (Λ, Σ, Ξ) can and do differ (Schaffner & Mishustin, 1996; Schaffner-Bielich & Gal, 2000). The present work adopts a uniform value of 0.9 as a simplification, aiming first to focus on the overall effects of the presence of hyperons. Investigating the differences in the couplings of different hyperons is an important direction for future research. In this work, we set $x_{\omega h}$=0.9, while $x_{\sigma h}$ is determined by fitting the hyperon potential well depth in saturated nuclear matter (Glendenning, 1997)

$$U_h^{(N)} = m_n \left(\frac{m_n^*}{m_n} - 1 \right) x_{\sigma h} + \left(\frac{g_\omega}{m_\omega} \right)^2 \rho_0 x_{\omega h}. \tag{17}$$

In this work, we adopt the hyperon potential depths $U_\Lambda^{(N)}$ = -30 MeV (Schaffner-Bielich & Gal, 2000; Weissenborn et al., 2012; Gal et al., 2016), $U_\Sigma^{(N)}$ = 30 MeV (Schaffner-Bielich & Gal, 2000; Weissenborn et al., 2012; Gal et al., 2016; Batty et al., 1997), and $U_\Xi^{(N)}$ = -14 MeV (Harada et al., 2010).

We take the coupling parameters between the mesons σ^* and ϕ and the hyperons as (Schaffner et al., 1994)

$$g_{\phi\Xi} = 2g_{\phi\Lambda} = 2g_{\phi\Sigma} = -2\sqrt{2}g_\omega/3, \tag{18}$$

$$g_{\sigma^*\Lambda}/g_\sigma = g_{\sigma^*\Sigma}/g_\sigma = 0.69, \tag{19}$$

$$g_{\sigma^*\Xi}/g_\sigma = 1.25. \tag{20}$$

The temperature parameter in PNS models plays a dual role: it strongly influences local energy density and pressure through the T^4 term, while the structure

of the TOV equations may render the overall macroscopic properties less sensitive to it. For example, in earlier calculations (Zhao et al., 2025), when the temperature of the PNS was raised from 14 MeV to 21 MeV, the central energy density decreased from 1.028×10^{15}g cm^{-3} to 1.019×10^{15}g cm^{-3} (by 0.9%), and the central pressure decreased from 2.178×10^{35}dyne cm^{-2} to 2.118×10^{35}dyne cm^{-2}d (by 6%). In contrast, the computed maximum mass increased from 2.2562 $M_\odot$ to 2.2576 $M_\odot$ (a rise of 0.0014 $M_\odot$), representing only a 0.06% increase. In the present work, the temperature of the PNSs is chosen as T=15 MeV (Burrows & Lattimer, 1986). The chosen temperature of $T = 15$ MeV in this study corresponds to the typical physical conditions within the PNS core during the initial tens of seconds following a supernova explosion. This temperature value is based on the standard understanding of PNS evolution. Simulation studies indicate that at this stage, due to neutrino trapping and strong compression, the PNS core can reach temperatures of 10–30 MeV (Pons et al., 1999; Keil et al., 2003). When investigating neutrino processes, the EoS , and nucleosynthesis inside a PNS, the range of 10–20 MeV is widely considered as the characteristic temperature range (Hempel & Schaffner-Bielich, 2010; Roberts et al., 2012). Therefore, the selection of $T = 15$ MeV aims to represent this high-energy, high-density environment, in order to explore the behavior of relevant nuclear processes under astrophysical conditions.

In 2019, precise measurements of the NS PSR J0030+0451 were obtained. Riley et al. reported a mass $M = 1.34^{+0.15}_{-0.16}$ $M_\odot$ and a radius $R = 12.71^{+1.14}_{-1.19}$ km (Riley et al., 2019), while Miller et al. found $M = 1.44^{+0.15}_{-0.14}$ $M_\odot$ and $R = 13.02^{+1.24}_{-1.06}$ km (Miller et al., 2019). The accurate determination of its mass and radius is highly significant, providing a key observational constraint for selecting viable equations of state (EoS) in NS modeling

The mass values (or maximum masses) of PNSs as functions of radius are presented in Fig. 1. The four thick lines correspond to the PNS masses associated with PSR J0740+6620, PSR J0348+0432, PSR J1614-2230, and PSR J0737-3039A, respectively. The results show that only the TW99, DD-ME1, and GM1 models can reproduce the masses of all these four PNSs. The mass–radius relations predicted by TW99, DD-ME1, and GM1 are displayed in the right panel of Fig. 1. It can be seen that for a given mass, there exist two radii, among which the radii on the left side of the mass peak belong to the unstable non-physical branch, while those on the right side belong to the stable physical branch. Due to the residual high thermal pressure and particle components that have not fully reached β-equilibrium inside the PNS, its radius during the early evolutionary stages (e.g., 10–30 seconds after birth) is expected to be 10%–30% larger than that of its cold NS counterpart of the same mass (Burrows & Lattimer, 1986; Pons et al., 1999; Zhao, 2011). This difference serves as an important testable feature linking PNS evolutionary theory with observations of cold NSs. We see that the mass and radius of the PNS given by the GM1 model agree best with the results from Riley et al. and Miller et al. (see the shaded region in the

right panel of Fig. 1) among these models. Therefore, in this work, the GM1 model is adopted to investigate the effect of hyperon interactions on the surface gravitational redshift of PNSs.

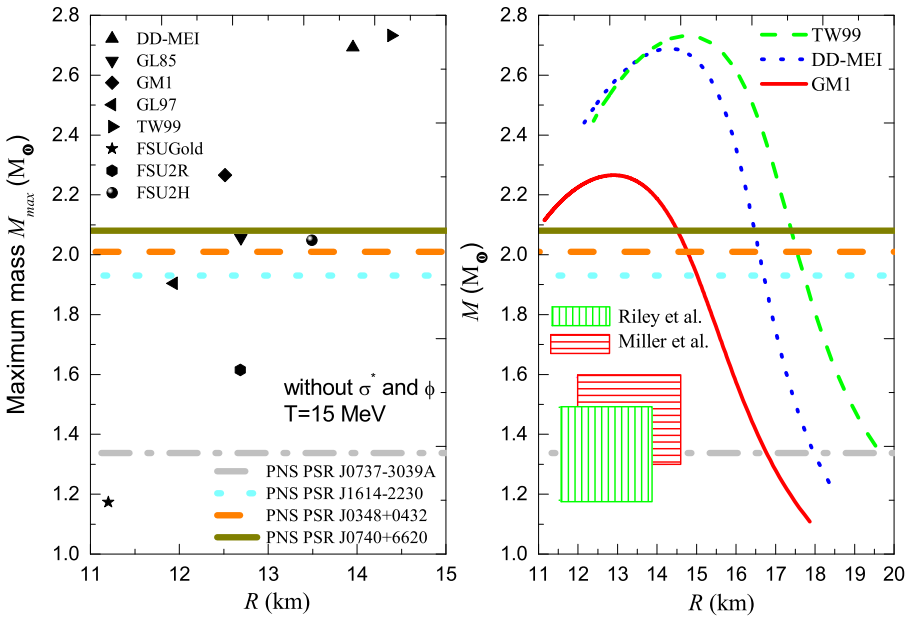

Figure 1. The mass M (or maximum mass M_{max}) of the PNS as a function of its radius R. The four thick lines correspond to the masses of the PNSs for PSR J0740+6620, PSR J0348+0432, PSR J1614–2230, and PSR J0737–3039A, respectively.

4. Mass and radius of PNSs

Figure 2 shows the radius R and mass M of a PNS as functions of the central energy density ε_c, calculated using the GM1 EoS. The four thick horizontal lines indicate the measured masses of the observed pulsars PSR J0740+6620, PSR J0348+0432, PSR J1614-2230, and PSR J0737-3039A, respectively. Solid red curves correspond to models without hyperon–hyperon interactions, while dashed green curves represent models that include these interactions.

Figure 2 shows that the mass M of the PNS increases while the radius R decreases with increasing central energy density ε_c. When hyperonic interactions are included, the mass M of the PNS decreases and its radius R increases at the same central energy density ε_c relative to the case without such interactions

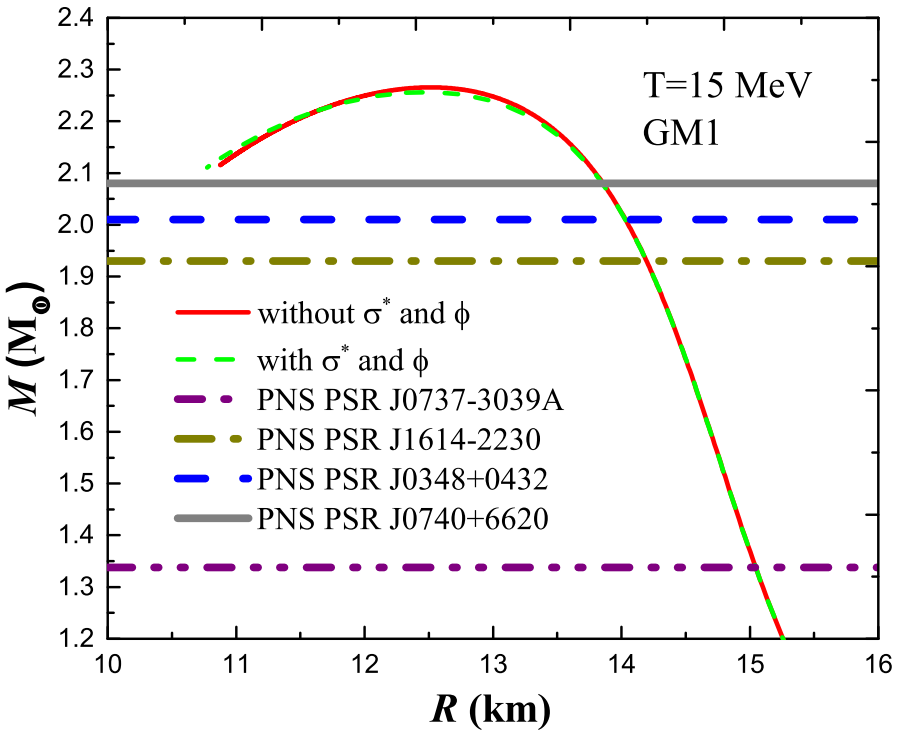

Figure 2. The mass M of a PNS as functions of radius R calculated within the GM1 EOS. The four thick horizontal lines mark the measured masses of the observed pulsars PSR J0740+6620, PSR J0348+0432, PSR J1614-2230, and PSR J0737-3039A, respectively. Solid red curves correspond to models without hyperon–hyperon interactions; dashed green curves include hyperon–hyperon interactions.

Under the constraints provided by the respective masses of the PNSs PSR J0740+6620, PSR J0348+0432, PSR J1614-2230, and PSR J0737-3039A (see Table 1), and when hyperonic interactions are considered, the radius of PSR J0740+6620 decreases from $R = 13.858$ km to $R = 13.849$ km, a reduction of about 0.065%. The radius of PSR J0348+0432 decreases from $R = 14.031$ km to $R = 14.029$ km, or about 0.014%. The radii of PSR J1614-2230 and PSR J0737-3039A remain unchanged at $R = 14.199$ km and $R = 15.05$ km, respectively (see Table 1). These results suggest that the reduction in radius due to hyperonic interactions is larger for more massive PNSs, while for less massive PNSs the effect on the radius is negligible.

Table 1. The calculated physical quantities of PNSs. The masses of PSR J0740+6620 (hereafter J0740+6620), PSR J0348+0432 (J0348+0432), PSR J1614-2230 (J1614-2230), and PSR J0737-3039A (J0737-3039A) are $M = 2.08$ $M_\odot$, $M = 2.01$ $M_\odot$, $M = 1.93$ $M_\odot$, and $M = 1.338$ $M_\odot$, respectively. The corresponding radius R, central energy density ε_c, central pressure p_c, compactness M/R, and surface gravitational redshift z are derived for each star. The units are as follows: R in km, ε_c in 10^{15} g·cm^{-3}, p_c in 10^{35} dyne·cm^{-2}, and M/R in $M_\odot$/km. These results are obtained using the GM1 nucleon coupling constant and assuming a uniform temperature of $T = 15$ MeV for all PNS models..

Parameter	R	ε_c	p_c	M/R	z
J0740+6620					
Withoutσ^* and ϕ	13.858	1.0202	2.1650	0.15009	0.3404
With σ^* and ϕ	13.849	1.0290	2.1798	0.15019	0.3402
Rate of variation	-0.065%	0.980%	0.739%	0.067%	-0.059%
J0348+0432					
Without σ^* and ϕ	14.031	0.9339	1.8300	0.14325	0.3168
With σ^* and ϕ	14.029	0.9365	1.8322	0.14327	0.3167
Rate of variation	-0.014%	0.644%	0.120%	0.014%	-0.032%
J1614-2230					
no σ^* and ϕ	14.199	0.856	1.533	0.1358	0.2921
with σ^* and ϕ	14.199	0.857	1.533	0.1358	0.2921
Rate of variation	0	0.117%	0%	0%	0%
J0737-3039A					
no σ^* and ϕ	15.05	0.563	0.553	0.0887	0.1639
with σ^* and ϕ	15.05	0.563	0.553	0.0887	0.1639
Rate of variation	0%	0%	0%	0%	0%

5. Energy density and pressure in PNSs

Figure 3 shows the pressure p of the PNS as a function of energy density ε. The thick vertical lines indicate the central energy densities ε_c for the PNSs of PSR J0740+6620, PSR J0348+0432, PSR J1614–2230, and PSR J0737–3039A. Solid lines correspond to models without hyperon interactions, and dashed lines to those with hyperon interactions included. It can be seen that p generally increases with ε. When hyperon interactions are considered, however, p is reduced at a given ε compared to the case without such interactions.

Constrained by the mass of the corresponding PNSs, and given the interactions between hyperons, the central pressure of PNS PSR J0740+6620 increases from p_c= 2.1650× 10^{35}dyne.cm^{-2} to p_c=2.1798× 10^{35} dyne.cm^{-2}, increased by about 0.739%; the central pressure of PNS PSR J0348+0432 increases from

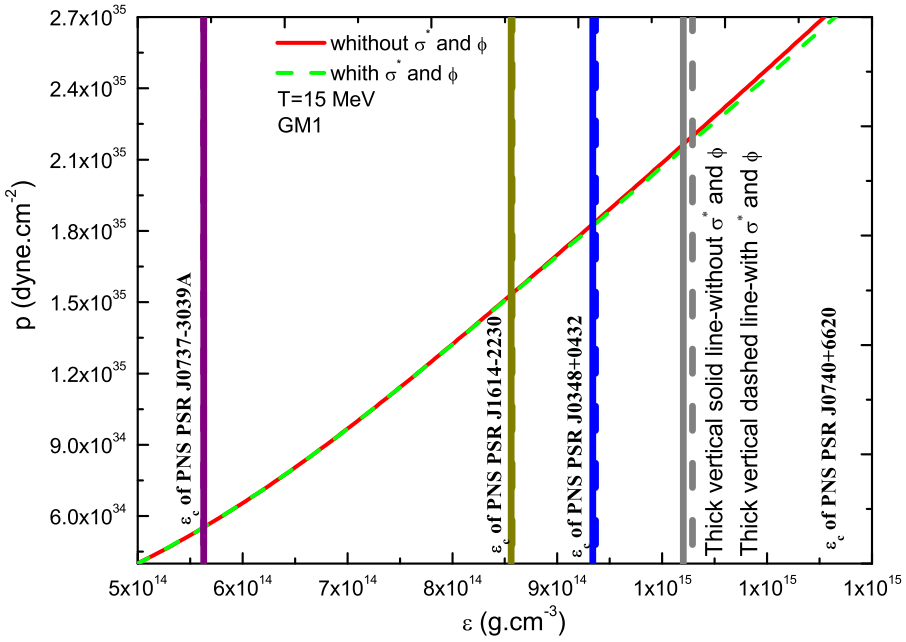

Figure 3. The pressure p of the PNS as a function of the energy density ε. The vertical thick lines mark the central energy densities ε_c of the PNSs for PSR J0740+6620, PSR J0348+0432, PSR J1614–2230, and PSR J0737–3039A, respectively. Solid vertical lines correspond to models without hyperon interactions, and dashed vertical lines correspond to models with hyperon interactions included.

p_c=1.8300 $\times 10^{35}$ dyne.cm^{-2} to p_c=1.8322$\times$ 10^{35} dyne.cm^{-2}, increased by about 0.120%; the central pressures of PNSs PSR J1614-2230 and PSR J0737-3039A respectively are p_c=1.533$\times$ 10^{35}dyne.cm^{-2} and p_c=0.533$\times$ 10^{35} dyne.cm^{-2}, no change. A similar conclusion holds for the central energy density ε_c. From this, we conclude that the larger the mass of the PNS, the greater the increase of the central pressure and the central energy density of the PNS due to the interaction between hyperons; for the PNS with reduced mass, this effect can be ignored.

6. The surface gravitational redshift of PNSs

Figure 4 presents the compactness M/R of the PNS as a function of the central energy density ε_c. The thick vertical lines indicate the central energy densities ε_c corresponding to the PNSs of PSR J0740+6620, PSR J0348+0432, PSR J1614-2230, and PSR J0737-3039A. Among these, the solid vertical lines denote cases without considering hyperon interactions, while the dashed vertical lines

represent cases with hyperon interactions included. It can be observed that the compactness M/R of the PNS increases with rising central energy density ε_c. When hyperon interactions are taken into account, the compactness M/R is reduced.

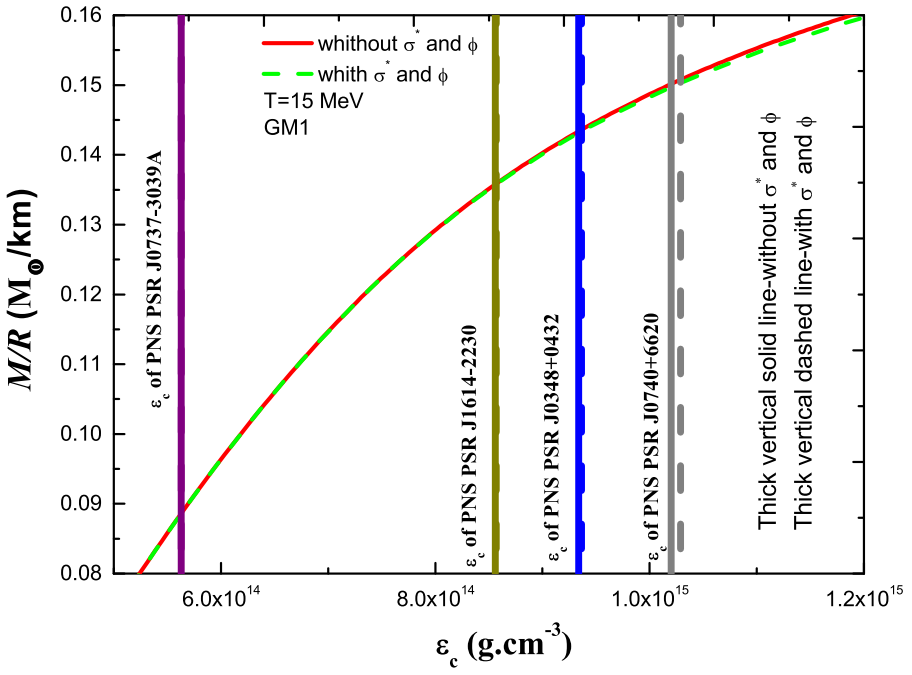

Figure 4. The compactness M/R of the PNS as a function of the central energy density ε_c . The thick vertical lines indicate the central energy densities ε_c of the PNSs corresponding to PSR J0740+6620, PSR J0348+0432, PSR J1614-2230, and PSR J0737-3039A, respectively. The solid vertical lines represent cases without hyperon interactions, while the dashed vertical lines represent cases with hyperon interactions.

Under the mass constraints imposed by the observed pulsars PSR J0740+6620, PSR J0348+0432, PSR J1614-2230, and PSR J0737-3039A, and when hyperon-hyperon interactions are included, the compactness M/R exhibits the following changes: for PSR J0740+6620, it increases from 0.15009 $M_\odot$/km to 0.15019 $M_\odot$/km, a relative increase of approximately 0.067%; for PSR J0348+0432, it increases from 0.14325 $M_\odot$/km to 0.14327 $M_\odot$/km, corresponding to a 0.014% increase. The compactness values for PSR J1614-2230 and PSR J0737-3039A remain unchanged. These results indicate that the effect of hyperon interactions on the compactness is negligible for lower-mass PNSs

Figure 5 shows the surface gravitational redshift z of the PNS as a function of the central energy density ε_c. It can be seen that the surface gravitational redshift z of the PNS increases with the central energy density ε_c. When hyperonic interactions are taken into account, the surface gravitational redshift z of the PNS is reduced at the same central energy density ε_c.

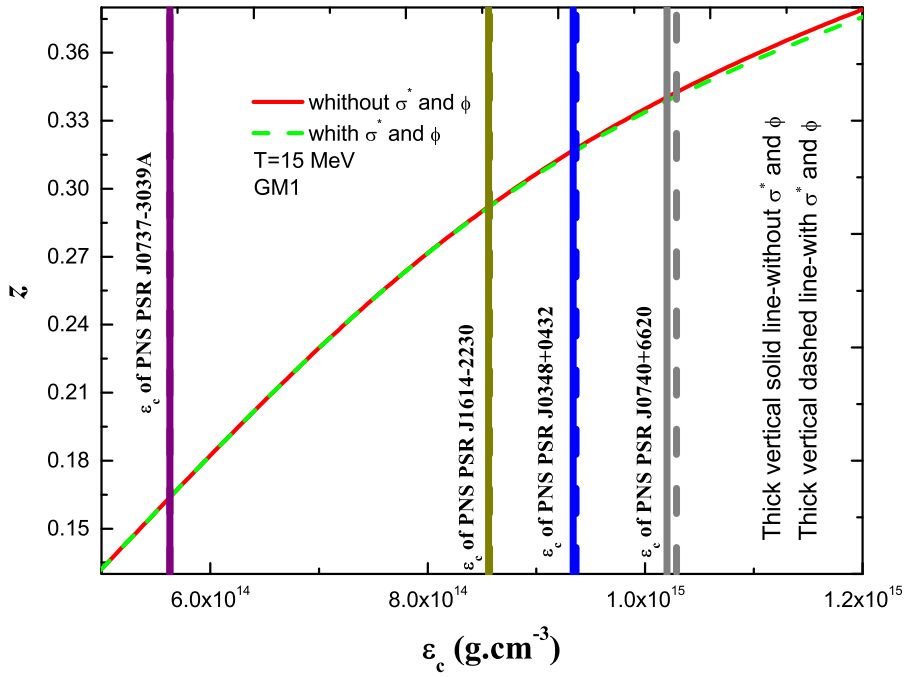

Figure 5. Surface gravitational redshift z of the PNS as a function of central energy density ε_c. The thick vertical lines indicate the central energy densities ε_c for the PNS models of PSR J0740+6620, PSR J0348+0432, PSR J1614-2230, and PSR J0737-3039A, with solid and dashed lines corresponding to models without and with hyperonic interactions, respectively.

Under the constraints of the respective masses of the PNSs PSR J0740+6620, PSR J0348+0432, PSR J1614-2230, and PSR J0737-3039A, and considering the effect of hyperon interactions, the surface gravitational redshift of PSR J0740+6620 decreases from $z = 0.3404$ to $z = 0.3402$, corresponding to a reduction of approximately 0.059%. For PSR J0348+0432, the surface gravitational redshift increases from $z = 0.3168$ to $z = 0.3167$, which is a decrease of about 0.032%. In contrast, the surface gravitational redshifts of PSR J1614-2230 and PSR J0737-3039A remain unchanged. These results indicate that, for

lower-mass PNSs, hyperon interactions have almost no effect on the surface gravitational redshift.

Figure 6 shows the surface gravitational redshift z of the PNS as a function of its radius R . The symbols in the figure correspond to the surface gravitational redshifts of PNSs PSR J0740+6620, PSR J0348+0432, PSR J1614-2230, and PSR J0737-3039A, respectively. Here, solid symbols denote cases without hyperon interactions, while open symbols represent cases with hyperon interactions taken into account. It can be observed that the surface gravitational redshift of a PNS decreases with increasing radius. When hyperon interactions are considered, the surface gravitational redshift for a given radius is reduced.

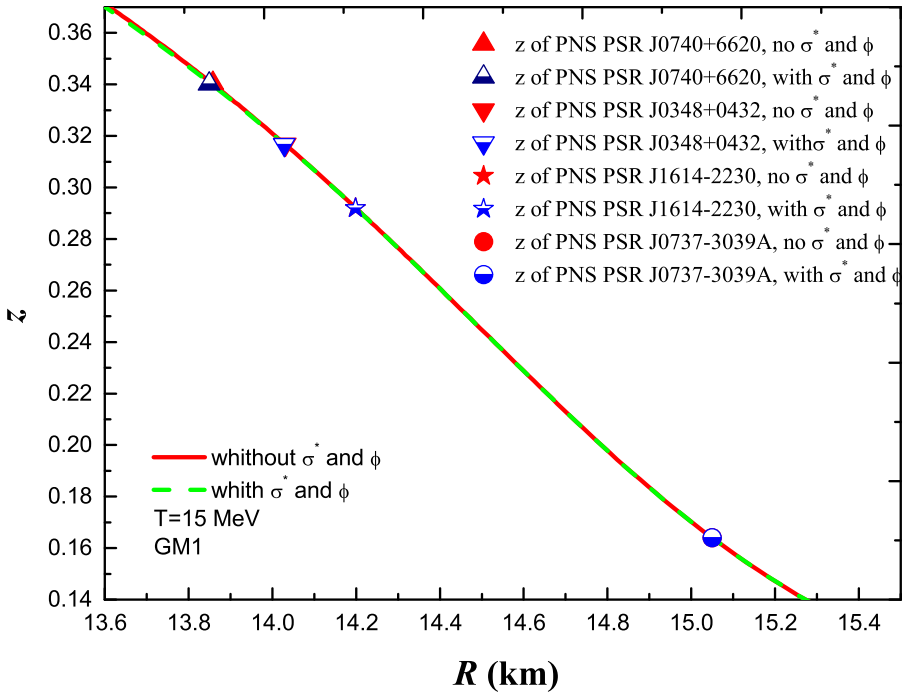

Figure 6. Surface gravitational redshift z of the PNS as a function of radius R . The symbols represent the values for PNSs PSR J0740+6620, PSR J0348+0432, PSR J1614-2230, and PSR J0737-3039A, respectively. Solid symbols correspond to cases without hyperon interactions, while open symbols denote cases with hyperon interactions included.

The surface gravitational redshift z of the PNS as a function of mass M is shown in Fig. 7. The four thick lines correspond to the masses of the PNSs PSR J0740+6620, PSR J0348+0432, PSR J1614-2230, and PSR J0737-3039A,

respectively. The solid red curves represent models without including hyperon interactions, whereas the dashed green curves represent those with hyperon interactions taken into account.

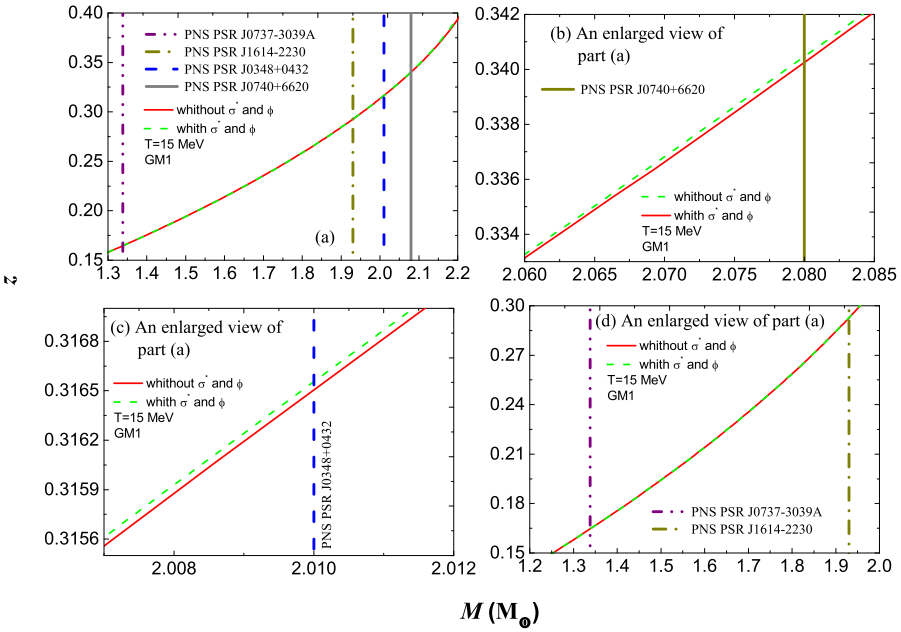

Figure 7. The surface gravitational redshift z of the PNS as a function of mass M. The four thick lines indicate the masses of the PNSs PSR J0740+6620, PSR J0348+0432, PSR J1614-2230, and PSR J0737-3039A, respectively. Solid red curves correspond to models without hyperon interactions, while dashed green curves correspond to models with hyperon interactions included.

From Fig. 7(a), it can be observed that the surface gravitational redshift z of the PNS increases with its mass M. When hyperon interactions are included, the surface gravitational redshift z increases—compared to models with the same mass M—for the PNSs PSR J0740+6620 and PSR J0348+0432 (see Figs. 7(b) and 7(c)). In contrast, the surface gravitational redshift z of the lower-mass PNSs PSR J1614-2230 and PSR J0737-3039A remains essentially unchanged.

7. Summary

In this paper, the effects of hyperon interactions on the surface gravitational redshift z of the PNSs PSR J0740+6620, PSR J0348+0432, PSR J1614-2230,

and PSR J0737-3039A are investigated within the RMF framework. The calculations adopt the nucleon coupling parameter set GM1 and assume a PNS temperature of $T = 15$ MeV.

As can be observed, the pressure p of the PNS increases with the energy density ε. When hyperon interactions are taken into account, the pressure p decreases at a given energy density ε. The increase in both central pressure and central energy density due to hyperon interactions becomes more pronounced for higher PNS masses. In contrast, for lower-mass PNSs, this effect is negligible.

As the central energy density ε_c increases, the mass M, the compactness M/R, and the surface gravitational redshift z of the PNS also increase, whereas its radius R decreases. When hyperon interactions are included, at a given ε_c, the values of M, M/R, and z are reduced.

For the higher-mass PNSs PSR J0740+6620 and PSR J0348+0432, the influence of hyperon interactions on the compactness M/R and the surface gravitational redshift z is significant. In contrast, for the lower-mass PNSs PSR J1614-2230 and PSR J0737-3039A, the effect of hyperon interactions on M/R and z is negligible.

A comprehensive assessment of PNS redshift requires considering rotation and rapid evolution. The current adoption of a static, spherically symmetric model represents a first-order approximation, aimed at focusing on constraining the core EoS. Rotation introduces anisotropy in the redshift and a dependence on the line-of-sight direction (Cadeau et al., 2005; Morsink et al., 2007), while time evolution leads to a significant increase in redshift over time and a 'time-averaging' effect in actual observations. These complex effects will be important directions for our future research.

Acknowledgements. This work was support by the Project of Science and Technology Strategic Cooperation between Nanchong City and SWPU of China (Grant No. SXHZ017), the Project of Science and Technology Strategic Cooperation between Nanchong City and SWPU of China (Grant No. SXHZ036), and the Natural Science Foundation of China (Grant No.12465023).

References

Antoniadis, J., Freire, P. C. C., et al., A Massive Pulsar in a Compact Relativistic Binary. 2013, *Science*, **340**, 448, DOI:10.1126/science.1233232

Batty, C. J., Friedman, E., & Gal, A., Strong interaction physics from hadronic atoms. 1997, *Phys. Rep.*, **287**, 385, DOI:10.1016/S0370-1573(97)00011-2

Burrows, A. & Lattimer, J. M., The Birth of Neutron Stars. 1986, *Astrophysical Journal*, **307**, 178, DOI:10.1086/164405

Cadeau, C., Leahy, D. A., & Morsink, S. M., Pulse Shapes from Rapidly Rotating Neutron Stars: Equatorial Photon Orbits. 2005, *The Astrophysical Journal*, **618**, 451, DOI:10.1086/425857

Chatterjee, D. & Vidana, I., Do hyperons exist in the interior of neutron stars? 2016, *The European Physical Journal A*, **52**, 29, DOI:10.1140/epja/i2016-16029-x

Cromartie, H. T., Fonseca, E., & Ransom, S. M., Relativistic Shapiro delay measurements of an extremely massive millisecond pulsar. 2020, *Nature Astronomy*, **4**, 72, DOI:10.1038/s41550-019-0880-2

Demorest, P. B., Pennucci, T., Ransom, S. M., Roberts, M. S. E., & Hessels, J. W. T., A two-solar-mass neutron star measured using Shapiro delay. 2010, *Nature*, **467**, 1081, DOI:10.1038/nature09466

Deng, Z. L., Li, X. D., & Gao, Z. F., Evolution of LMXBs under Different Magnetic Braking Prescriptions. 2021, *The Astrophysical Journal*, **909**, 174, DOI:10.3847/1538-4357/abe0b2

Ding, W. B., Cai, M. D., & Chan, A. H., The impact of dark matter on neutron stars with antikaon condensations. 2022, *International Journal of Modern Physics A*, **37**, 2250034, DOI:10.1142/S0217751X22500348

Fonseca, E., Pennucci, T. T., Ellis, J. A., et al., The NANOGrav Nine-year Data Set: Mass and Geometric Measurements of Binary Millisecond Pulsa. 2016, *The Astrophysical Journal*, **832**, 167, DOI:10.3847/0004-637X/832/2/167

Fonseca, E., T, C. E., T, P. T., et al., Refined Mass and Geometric Measurements of the High-mass PSR J0740+6620. 2021, *The Astrophysical Journal Letters*, **915**, L12, DOI:10.3847/2041-8213/ac03b8

Gal, A., Hungerford, E. V., & Millener, D. J., Strangeness in nuclear physics. 2016, *Reviews of Modern Physics*, **88**, 035004, DOI:10.1103/RevModPhys.88.035004

Glenden ning, N. K. & Moszkowski, S. A., Reconciliation of neutron-star masses and binding of the Lambda in hypernuclei. 1991, *Physical Review Letters*, **67**, 2414, DOI:10.1103/PhysRevLett.67.2414

Glendenning, N., Hot metastable state of abnormal matter in relativistic nuclear field theory. 1987a, *Nuclear Physics A*, **469**, 600, DOI:10.1016/0375-9474(87)90015-7

Glendenning, N. K., Neutron stars are giant hypernuclei ? 1985, *Astrophysical Journal*, **293**, 470, DOI:10.1086/163253

Glendenning, N. K., Finite temperature metastable matter. 1987b, *Physics Letters B*, **185**, 275, DOI:10.1016/0370-2693(87)90999-3

Glendenning, N. K. 1997 (New York, Inc.: Springer-Verlag)

Harada, T., Hirabayashi, Y., & Umeya, A., Production of doubly strange hypernuclei via Ξ^- doorways in the 16O (K^- ,K^+) reaction at 1.8 GeV/c. 2010, *Physics Letters B*, **690**, 363, DOI:10.1016/j.physletb.2010.05.053

Hempel, M. & Schaffner-Bielich, J., A statistical model for a complete supernova equation of state. 2010, *Nuclear Physics A*, **837**, 210, DOI:10.1016/j.nuclphysa.2010.02.010

Keil, M. T., Raffelt, G. G., & Janka, H. T., Monte Carlo Study of Supernova Neutrino Spectra Formation. 2003, *The Astrophysical Journal*, **590**, 971, DOI:10.1086/375130

Kramer, M., Stairs, I. H., Manchester, R. N., et al., Tests of General Relativity from Timing the Double Pulsar. 2006, *Science*, **314**, 97, DOI:10.1126/science.1132305

Li, Y., Chen, H., Wen, D., & Zhang, J., Constraining the nuclear symmetry energy and properties of the neutron star from GW170817 by Bayesian analysis. 2021, *European Physical Journal A*, **57**, 31, DOI:10.1140/epja/s10050-021-00342-w

Lyne, A. G., Burgay, M., et al., A Double-Pulsar System: A Rare Laboratory for Relativistic Gravity and Plasma Physics. 2004, *Science*, **303**, 1153, DOI:10.1126/science.1094645

Miller, M. C., Lamb, F. K., Dittmann, A. J., et al., PSR J0030+0451 Mass and Radius from NICER Data and Implications for the Properties of Neutron Star Matter. 2019, *The Astrophysical Journal Letters*, **887**, L24, DOI:10.3847/2041-8213/ab50c5

Miller, M. C., Lamb, F. K., Dittmann, A. J., et al., The Radius of PSR J0740+6620 from NICER and XMM-Newton Data. 2021, *The Astrophysical Journal Letters*, **918**, L28, DOI:10.3847/2041-8213/ac089b

Morrison, I. A., Baumgarte, T. W., Shapiro, S. L., et al., The Moment of Inertia of the Binary Pulsar J0737-3039A: Constraining the Nuclear Equation of State. 2004, *The Astrophysical Journal*, **617**, L135, DOI:10.1086/427235

Morsink, S. M., Leahy, D. A., Cadeau, C., et al., The Oblate Schwarzschild Approximation for Light Curves of Rapidly Rotating Neutron Stars. 2007, *The Astrophysical Journal*, **663**, 1244, DOI:10.1086/518648

Mu, X. L., Jia, H. Y., & Zhou, X. 2017, *The Astrophysical Journal*, **846**, 140, DOI:10.3847/1538-4357/aa880c

Oppenheimer, J. R. & Volkoff, G. M., On Massive Neutron Cores. 1939, *Physical Review*, **55**, 374, DOI:10.1103/PhysRev.55.374

Pons, J. A., Reddy, S., Prakash, M., Lattimer, J. M., & Miralles, J. A., Evolution of Proto-Neutron Stars. 1999, *The Astrophysical Journal*, **513**, 780, DOI:10.1086/306889

Riley, T. E., Watts, A. L., Bogdanov, S., et al., A NICER View of PSR J0030+0451: Millisecond Pulsar Parameter Estimation. 2019, *The Astrophysical Journal Letters*, **887**, L21, DOI:10.3847/2041-8213/ab481c

Roberts, L. F., Reddy, S., & Shen, G., Medium modification of the charged-current neutrino opacity and its implications. 2012, *Physical Review C*, **86**, 065803, DOI:10.1103/PhysRevC.86.065803

Romani, R. W., Kandel, D., Filippenko, A. V., et al., PSR J0952-0607: The Fastest and Heaviest Known Galactic Neutron Star. 2022, *The Astrophysical Journal Letters*, **934**, L17, DOI:10.3847/2041-8213/ac8007

Schaffner, J., Dover, C. B., Gal, A., et al., Multiply Strange Nuclear Systems. 1994, *Annals of Physics*, **235**, 35, DOI:10.1006/aphy.1994.1090

Schaffner, J. & Mishustin, I. N., Hyperon-rich matter in neutron stars. 1996, *Physical Review C*, **53**, 1416, DOI:10.1103/PhysRevC.53.1416

Schaffner-Bielich, J. & Gal, A., Properties of strange hadronic matter in bulk and in finite systems. 2000, *Physical Review C*, **62**, 034311, DOI:10.1103/PhysRevC.62.034311

Todd-Rutel, B. G. & Piekarewicz, J., Neutron-Rich Nuclei and Neutron Stars: A New Accurately Calibrated Interaction for the Study of Neutron-Rich Matter. 2005, *Physical Review Letters*, **95**, 122501, DOI:10.1103/PhysRevLett.95.122501

Tolman, R. C., Static Solutions of Einstein's Field Equations for Spheres of Fluid. 1939, *Physical Review*, **55**, 364, DOI:10.1103/PhysRev.55.364

Tolos, L., Centelles, M., & Ramos, A., The Equation of State for the Nucleonic and Hyperonic Core of Neutron Stars. 2017, *Publications of the Astronomical Society of Australia*, **34**, e065, DOI:10.1017/pasa.2017.60

Typel, S. & Wolter, H. H., Relativistic mean field calculations with density-dependent meson-nucleon coupling. 1999, *Nuclear Physics A.*, **656**, 331, DOI:10.1016/S0375-9474(99)00310-3

Weissenborn, S., Chatterjee, D., Schaffner-Bielich, J., et al., Hyperons and massive neutron stars: Vector repulsion and SU(3) symmetry. 2012, *Physical Review C*, **85**, 065802, DOI:10.1103/PhysRevC.85.065802

Zhao, X. F., Constraining the Surface Gravitational Redshift of Proto Neutron Stars with New Nucleon Coupling Constants. 2011, *International Journal of Theoretical Physics*, **50**, 2951, DOI:10.1007/s10773-011-0795-x

Zhao, X. F., The Composition of Baryon in the Proto Neutron Star PSR J0348+0432. 2019, *International Journal of Theoretical Physics*, **58**, 1060, DOI:10.1007/s10773-018-03997-2

Zhao, X. F., Ding, W. B., & Tang, B., Temperature Effects in the Proto Neutron Star Phase of PSR J0740+6620. 2025, *Astrophysics*, **68**, 403, DOI:10.1007/s10511-025-09885-y

Zhou, S. G., Multidimensionally constrained covariant density functional theories-nuclear shapes and potential energy surfaces. 2016, *Physica Scripta*, **91**, 063008, DOI:10.1088/0031-8949/91/6/063008